



Study of the current density of the electrical resistance sintering technique on microstructural and mechanical properties in a β Ti-Nb-Sn ternary alloy

Mariana Correa Rossi¹ · Eber de Santi Gouvêa¹ · Montserrat Vicenta Haro Rodríguez¹ · Margarida Juri Saeki² · Angel Vicente Escuder¹ · Vicente Amigó Borrás¹

Received: 10 June 2021 / Accepted: 16 September 2021 / Published online: 28 September 2021
© The Author(s), under exclusive licence to Springer-Verlag GmbH, DE part of Springer Nature 2021

Abstract

Electrical resistance sintering is a fast method to fabricate metallic samples in the metallurgy field and was used to obtain the Ti-Nb-Sn alloy to be applied as a possible biomaterial. Powders were obtained by mechanical alloying and were then compacted at 193 MPa pressure for 700 ms at several electrical current densities (11, 12 and 13 kA). The structure and microstructure of both powders and samples were evaluated by X-ray diffraction, Field Emission Scanning Electron Microscopy and Electron Backscattered Diffraction. Mechanical properties were evaluated by a microhardness assay and corrosion resistance was performed in Ringer Hartmann's solution at 37°C. Samples were structured in the α , α'' and β phases. The content of the β phase in the samples obtained at 11, 12 and 13 kA was 96.56, 98.12 and 98.02%, respectively. The peripheral zone showed more microporosity than the central zone. The microstructure was also formed by equiaxial bcc- β grains, and the samples obtained at 12 kA presented better microstructure homogeneity. Grain size increased as electric current density rose. The microhardness values fell within the 389–418 HV range and lowered, while electric current density increased. Corrosion tests proved the alloys' excellent corrosion resistance (0.24–0.45 $\mu\text{A}/\text{cm}^2$). The standard deviations of the kinetic parameters of the samples at 11 and 13 kA were much higher in relation to lack of microstructure homogeneity.

Keywords ERS · Mechanical alloying · β -Ti alloy · Corrosion resistance · Biomaterial

1 Introduction

Studies about metallic alloys based on titanium (Ti) for applications in orthopedics are a constantly developing field due to the inconveniences of commercial metallic prostheses that lead to long-term failure and to rejection by the body. The main features required to make these biomaterials successful are non-toxicity, good corrosion resistance and an elastic modulus close to bone tissue [1–3]. Metallic materials based on cobalt (Co), chromium (Cr), aluminum (Al), vanadium (V) and nickel (Ni) are known to exhibit

allergenic and carcinogenic effects, as well as proven respiratory and neurological disorders [4, 5]. Corrosion resistance is closely linked with the chemical composition of these materials, such as the content of elements stabilizing the hcp (α phase) and bcc (β phase) crystalline structures, and the type of processing employed, which will interfere with their microstructure and morphology. Most employed materials have higher elastic modulus values than that of bone tissue, such as Co-Cr, Ti-6Al-4 V or Ti-CP alloys [6, 7]. This difference leads to adaptive bone resorption, which lasts for 10 to 15 years, when the patient needs surgery to repair and replace the prosthesis [8]. This phenomenon arises due to the cushioning effect, whereby bone absorbs all the charge loaded on the prosthesis because its elastic modulus is larger. Bone is daily discouraged and its fragility intensifies around the implant, which means losing prosthesis stability, and these effects are not observed in the short-term. However, a prosthesis that requires bone healing, which will be inserted and left in the patient for life, tends to fail when faced with this problem. In order to repair such inconveniences,

✉ Mariana Correa Rossi
mrncorrea90@gmail.com

¹ Institut de Tecnologia de Materials, Universitat Politècnica de València, Camí de Vera s/n, 46022 Valencia, Spain

² Department of Chemistry and Biochemistry, Institute of Biosciences (IBB), São Paulo State University, Botucatu, Brazil

Ti alloys based on niobium (Nb) and tin (Sn) have been studied as it is known Nb (β isomorphic stabilizer, space group: Im-3 m) and Sn (neutral element, space group: 141/amd) are elements that do not present toxicity, and are good candidates for manufacturing Ti alloys with a lower elastic modulus [9] and good mechanical strength [10]. Based on a phase diagram of the Ti-Nb binary system [11], Nb exhibits complete solubility in Ti above 882 °C, which allows its influence on the entire range of Nb content in a system to be studied, and to also observe the modification of its properties by the diffusion process [11, 12]. At a lower temperature, it is possible to note two stable phases ($\alpha + \beta$), but the rapid cooling of the phase β results in a structure composed of metastable phases. With the Ti-Nb system, this sudden cooling results in the martensitic transformation of the β phase, which can result in the α' or α'' phases depending on Nb content [13]. The effects of Nb content on the mechanical properties of the Ti-Nb alloy and its relation to the β phase content were evaluated by Yahaya et al., 2016, by preparing these alloys by powder metallurgy (PM) [14]. Those authors found that up to 35% (wt%) of Nb, the alloy did not crystallize as the α phase. However, higher Nb contents, such as 45% (wt%), resulted in less mechanical resistance to compression despite a lower elastic modulus (13.46GPa). In general, the alloy with 35 (wt%) of Nb presented the most adequate characteristics regarding the microstructure and mechanical properties. In most works, Ti-Nb-Sn alloys were manufactured following spark plasma sintering (SPS) and conventional powder metallurgy (PM) to prepare them. Thus studies on the preparation of these materials by an electrical resistance-based sintering technique (ERS) are lacking. The first patent for electric current sintering was registered in 1906 by Lux [15]. Some years later came Taylor's [16] (in 1933) and Lenel's studies [17] (in the 1950s), who called this technique electrical pressure resistance sintering (EPRS). In the 1970s and 1980s, the ERS technique received a new boost, mainly by Soviet and Japanese researchers [18, 19]. Nowadays, the ERS technique is studied as an electrical field-assisted sintering technique (FAST) modality, which is the common name for the technique based on the electrical consolidation of powder metallurgy (PM). During this long period, many FAST variants have been developed to be applied on an industrial scale as their overall ultimate goal [20–22]. The most popular FAST is the so-called SPS, in which low-wear (electrically conductive) graphite dies and punches are used to combine the application of alternating current and vacuum or argon for atmospheric control.

The ERS technique allows durable electrical insulation matrices to be utilized, and the process can take place in air with a typical cycle being completed in seconds or milliseconds. In addition, the required equipment can be easily adapted from the well-known resistance welding technology, a well-tested technology.

Among the advantages of ERS compared to conventional PM we find the use of relatively low pressures (about 100 MPa) to obtain the final material with very high density, extraordinarily short processing times (about 1 s or less) and the possibility of operating in air without the need for a controlled atmosphere [23, 24]. The main disadvantages of the ERS technique arise from operational difficulties (incomplete knowledge of parameters and how certain parameters influence the process) and non-homogenous temperature distribution in the powder mass [25]. Recent studies have shown excellent results of the mechanical (low elastic modulus and mechanical resistance close to bone tissue) and biological (non-cytotoxicity and induction of osteogenic differentiation) compatibility of TiNbSn (34 wt% Nb and 6wt% Sn). [26, 27], and in comparison with TiNbSn alloys with different compositions, such as Ti-30Nb-xSn (x = 4 and 5 wt%) and Ti-25Nb-11Sn [28–30].

Li et al., 2019 observed increasing Nb content, and how the α'' martensite phase decreased, which is unfavorable in Ti alloys [31]. In the same work, the obtained hardness values fell within the 218–230HV range depending on Nb content. It is noteworthy that the composition did not exceed 20 wt% Nb, and Sn content was set at 5 wt%. The same work also confirmed that employing low Sn contents (up to 10wt%) also reduced the formation of the α'' martensite phase [32, 33]. The main obstacles brought about by the presence of the α'' martensite phase was the reduced volumetric fraction of the β phase, which also had a negative effect on the alloy's superelastic and ductility properties [34]. Indeed 34 wt% Nb and 6 wt% Sn were chosen to obtain an alloy with higher β phase levels, which came close to the physical and mechanical parameters of bone tissue, besides being explored by our research group in other published works. In order to increase knowledge about the ERS process in preparing β -Ti alloys, a study was carried out on the influence of electric current on the microstructural, physical, mechanical and electrochemical properties of the promising Ti-34Nb-6Sn alloy for its use as a medical implant.

2 Materials and methods

2.1 Powders preparation

The elemental powders of Ti (99.9%), Nb (99.8%) and Sn (99.8%) were purchased from Atlantic Equipment Engineers, with particle sizes of around 30, 16 and 17 μm , respectively. They were weighed to obtain alloys with 34 (wt%) Nb and 6 (wt%) Sn in a glove box to minimize oxygen and nitrogen contamination.

Then they were mixed with a process control agent (PCA), NaCl (in powder), whose amount was 1.5 (wt%) in relation to the total mass of powders. The use of NaCl

as PCA was to avoid an excessive cold-welding effect during high-energy milling, which has an active surface, and contributes to obtain the nanocrystalline microstructure. The mixture was made for 30 min in a tumbler mixer (Inversina 2L-Bioengineering AG) at 90 rpm, followed by a 72-h milling process to promote mechanical alloying. The milling process was carried out at room temperature in a high-energy mill (Retsch- PM 400/2) for 72 h at 240 rpm, interspersed with 10 s of rest for every 8 min of milling break. Before starting the process, the steel vessel was purged by argon 4 times. The employed ratio of steel balls (5 mm radius) to the powder mass was 10:1.

2.2 Synthesis via ERS

Specimen consolidation was carried out by the ERS technique in equipment developed as part of the EU funded EFFIPRO project (Fig. 1), used in collaboration with the AMES Company (Barcelona-ES). Materials were produced in a cylindrical matrix (diameter of 2.2 cm, thickness of 0.55 cm).

In order to obtain samples with these dimensions, the alloy's density ($\rho_{\text{Ti}_{34}\text{Nb}_{6}\text{Sn}} = 5.52 \text{ g/cm}^3$) was taken into account to calculate the powder mass according to Eq. 1 below.

$$\rho_{\text{Ti}_{34}\text{Nb}_{6}\text{Sn}} = \frac{100}{\left(\frac{C}{\rho}\right)_{\text{Ti}} + \left(\frac{C}{\rho}\right)_{\text{Nb}} + \left(\frac{C}{\rho}\right)_{\text{Sn}}} \quad (1)$$

where C is the concentration of the element (wt %) and ρ is the specific density of the element, expressed as g/cm^3 .

The mixture powder was placed in a silicon nitride die between two tungsten-copper electrodes [35] and compacted at 193 MPa pressure. The current intensities tested for consolidation were 11, 12 and 13 kA for a sintering time of 700 ms.

2.3 Phase/chemical and microstructural characterization

For the characterization and evolution of the current phases, as well as the lattice parameters of powders, X-ray diffraction (XRD) was applied (Bruker/D2Phaser). Cu K α radiation ($\lambda = 1.541 \text{ \AA}$) was used, which works at 30 kV and 10 mA. The XRD measurement was taken within the 20–90 deg range with a 0.02° step every 10 s. Structure refinement and the quantitative phase analysis were carried out by the free MAUD software (version 2.94). Phases and diffraction planes were analyzed by comparing the d value of each peak of the diffraction pattern from those of the Inorganic Crystal Structure Database (ICSD). In addition, crystallite size and the induced micro-strain in the Ti lattice were calculated from the peak broadening and peak positioning of the X-ray diffraction pattern of the milled powder and the sintered samples according to the Williamson-Hall equation [36].

$$\beta \cos \theta = \frac{k\lambda}{D} + 4\varepsilon \sin \theta \quad (2)$$

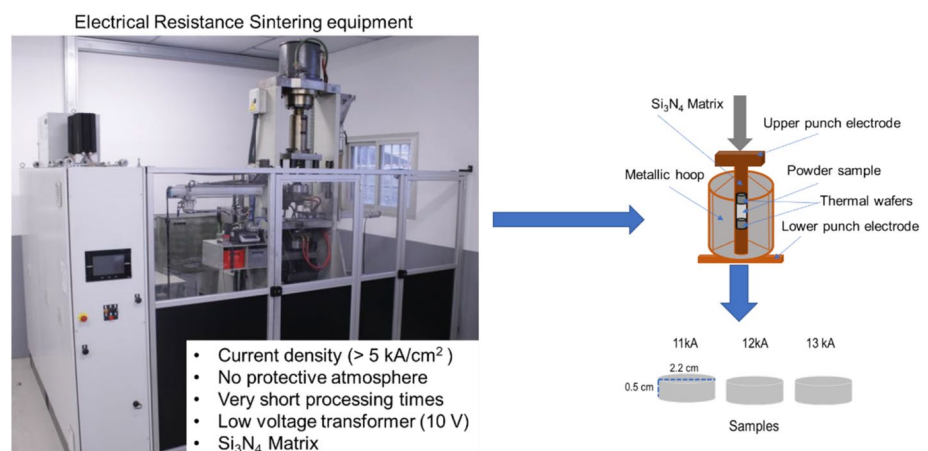
where β = dull width at half maximum, k = shape factor generally taken as 0.9 [37], λ = wave length of the radiation used in XRD, Θ = Bragg's angle, D = crystalline size and ε = induced strain in the lattice. The graph was plotted between $4 \sin \Theta$ and $\beta \cos \Theta$ for the selected peaks of the powder sample along the x-axis and the y-axis, respectively. A best fitted linear curve was drawn for the different Ti peaks. Refinement quality was calculated by the weighted-profile R value (R_{wp}), which can be described as:

$$R_{wp} = 100 \sqrt{\frac{\sum_i \omega_i (Y_{oi} - Y_{ci})^2}{\sum_i \omega_i Y_{oi}^2}} \quad (3)$$

where ω_i is a weight associated with each Y_{oi} observed intensity and Y_{ci} is the corresponding calculated intensity.

Particle size distribution was measured in a particle size analyzer by laser scattering (Mastersizer 2000-Malvern

Fig. 1 Detailed diagram of the ERS process for the obtained samples



Instruments). Distilled water was used to disperse powders. The LECO TCH600 series equipment with an inert gas fusion analyzer was used to evaluate oxygen and nitrogen contamination.

The microstructure of powders after the MA process and of the sintered powders was characterized by Field Emission Scanning Electron Microscopy (FE-SEM) (ZEISS-ULTRA 55) with backscattered electrons (BSE), secondary electrons (SE) and X-ray energy dispersive detectors (EDS) (Oxford Instruments Ltd.). To more precisely characterize the microstructure, as with the grains and the phase quantifications, electron backscattered diffraction (EBSD) with a scanning electron microscope (Zeiss-ULTRA 55 operating at 20 kV) equipped with an Aztec HKL Max System (Oxford Instruments Ltd.) was applied at an acceleration voltage of 20 kV with a 0.1 μm step size by selecting the three possible phases to be analyzed: β -Ti, α -Ti and α'' -martensite. For powders, they were embedded in resin and metallographically prepared from cross section to analyze particle size, the homogeneity of the Ti, Nb and Sn elements and evolution microstructure.

2.4 Microhardness test

Vickers microhardness tester (HMV-SHIMADZU) was used to evaluate the samples consolidated by ERS. To measure microhardness, 12 indents were made on the surface of each sample by applying 490.3 mN (HV 0.05) for 12 s. For each indent, a distance of 50 μm was employed. Data were represented as mean \pm standard deviation.

2.5 Corrosion resistance in Ringer Hartmann's solution

Corrosion behavior was studied by measuring the open circuit potential (OCP) for 35 min and the potentiodynamic polarization assay after that time in a potentiostat/galvanostat 144 (Metrohm potentiostat-PGSTAT204) on a surface measuring 0.785 cm^2 using a conventional three-electrode cell in Ringer Hartmann's solution ($6 < \text{pH} < 7$) (NaCl 5.7 g/L, KCl 0.358 g/L, CaCl_2 0.221 g/L, lactate 4.956 g/L) at 37 $^\circ\text{C}$. The Ag/AgCl electrode was taken as the reference electrode and the Pt thread as the auxiliary one. All the potential values were expressed in relation to this reference electrode hereinafter, and the current density was normalized by the geometric area. The electrochemical tests consisted of OCP measurements (for 35 min) and polarization from OCP at the 2 mV/s scan rate. The corrosion parameters, such as Tafel slopes (b_a and b_c) in the region of the cathodic and anodic process domains, corrosion potential (E_{corr}) and corrosion current (I_{corr}), were determined by the Wolfram Mathematica 12.1 software. The Electrochemical Impedance Spectroscopy (EIS) technique was followed

within the 100 kHz–5 mHz frequency range with a sinusoidal amplitude wave of 0.01 V on E_{ocp} . For OCP, potentiodynamic polarization curves and EIS data were acquired during three experiments. Data were represented as mean \pm standard deviation.

3 Results and discussion

For the particle size analysis (shown in Table 1), the mixture showed a reasonably decreased particle size after the milling process by mechanical alloying (MA), with a similar obtained average as the initial size of Nb and Sn, but smaller than the initial Ti particles. The maximum particle size found was bigger than the initial size of the three elements (Ti, Nb, Sn), approximately 171 μm . It is known for certain that the MA process promotes not only a significant reduction particle size over time, but also their agglomeration due to the further interaction of the surface owing to a reduction in size. Another factor that contributes to the agglomeration process is the cold-welding effect, as well as the increase in temperature during the constant impacts of the balls and friction between balls and powders. PCA tends to diminish these effects. However, when employing this agent, the cold-welding process was difficult to control given the long milling time.

Partly due to the long milling time and the stronger impact of powders owing to shocks in vessel balls, agglomerated powders can contribute to decrease porosity to obtain higher density. A longer milling period can promote morphological changes in particles, which results in the creation of more spherical particles, which are more suitable for compaction and the sintering process.

The XRD pattern shown in Fig. 2 reveals that 72-h milling resulted in a material that was structured in two phases, namely: the α phase, represented by the compact hexagonal (hcp) structure, formed by a small peak that appeared around 35° , characterized by the plane (100) $_{\alpha}$; the β phase, represented by the body-centered cubic (bcc) structure. The milling process promoted almost 80% β phase formation (Table 2) due to the allotropic transformation achieved during MA by the diffusion of the Nb atoms in the Ti lattice.

Table 1 Particle size obtained after the MA process of Ti, Nb and Sn by laser scattering

Particle size	Minimum (μm)	Maximum (μm)	Average (μm)
Ti	11.06	29.23	55.93
Nb	2.53	15.94	45.00
Sn	6.19	16.94	52.32
Milled Powder 72 h	1.86	171.47	19.12

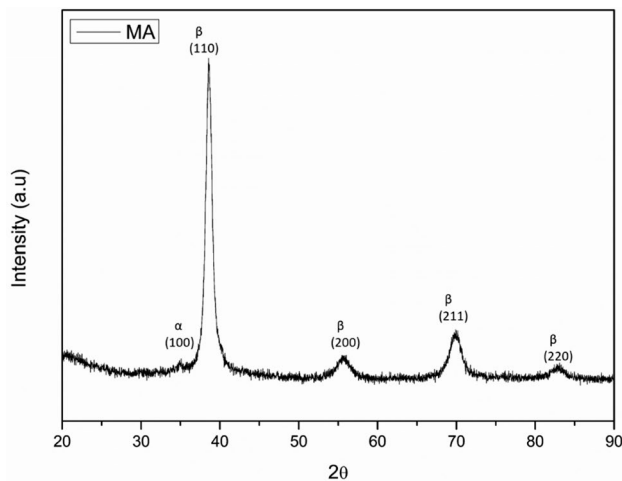


Fig. 2 The XRD pattern of powders after 72 h of MA

Table 2 Quantification of the phases present after the MA process obtained by structural refinement. The spectra Rietveld refinement analysis was performed by MAUD [40]. For phase identification, Powder Diffraction Files (PDF) entries 44–1294 and 44–1288 of the α phase and the β phase were, respectively, used. The PDF file of Tetragonal system of Sn (86–2264) was also employed to identify possible Sn peaks in the powder pattern. In order to obtain good quality structural refinement (RWP < 10%), each sample underwent five refinements by decreasing the background, in addition to changing the isotropic values to obtain a better fit. The RWP was calculated according to Eq. 3

Rwp (%)	α phase (%)	β phase (%)
5.8	22.1 ± 0.0	77.9 ± 5.8

Table 3 The O and N contents in powders after the MA process

Milled Powder	O (%)	N (%)
Ti-34Nb-6Sn	1.09 ± 0.04	0.216 ± 0.08

The α phase was present at approximately 22 wt%. The quality of the performed refinement, obtained by the weighted-profile R value (Rwp), was satisfactory (< 10%). O_2 and N_2 contents were evaluated after the milling process (see Table 3). The oxygen content values were reasonable for a long milling time compared to the Ti-Nb-based alloys within the 1.0–2.5 at% range [38, 39].

In Fig. 3, which refers to the cross section of powders, it is possible to note that after 72 h of milling, the Ti-34Nb-6Sn structure presented a small amount of typical microstructural composite particles represented by the white board, where the clearest contrast was found due to the presence of elements with a bigger atomic number, in this case Nb ($Z = 41$), and the darkest contrast indicates the zones richest in Ti. No isolated elemental particles (e.g.,

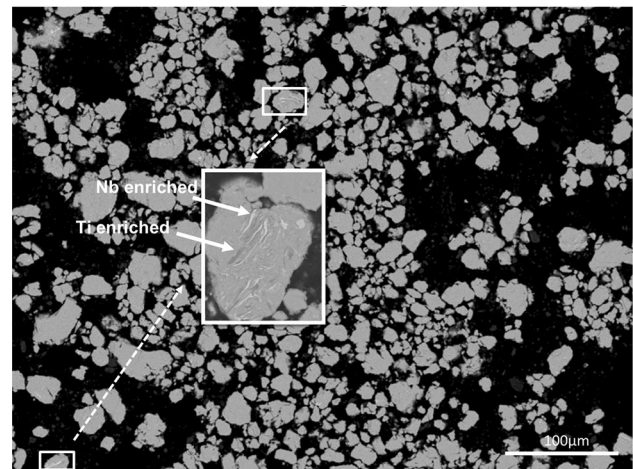


Fig. 3 SEM-backscattered electrons image of the cross section of powders after the 72-h milling process. White boards indicate typical microstructural composite particles

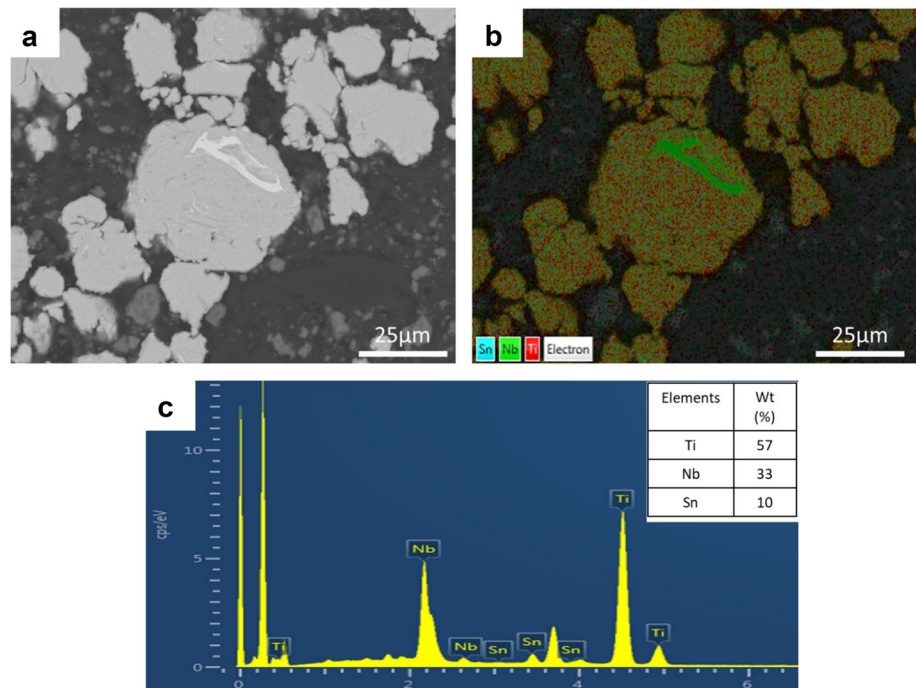
Ti, Nb or Ti) were found. This revealed the good homogeneity and uniformity of the formed microstructure. The applied milling time promoted good powder cracking, and decreased the surface area of an element's concentration.

We can clearly observe two distinct regions in the microstructure of the material after the milling process in Fig. 4a. Homogeneity of particles (Fig. 4b) is indicated by the map, with a good distribution of the three elements (Ti, Nb and Sn). These structures with suitable uniformity resemble a plate, which consists of a fine homogeneous distribution of the solute's components in the Ti matrix. The other region shows the presence of zones enriched by Nb and Ti, which did not react during the milling time, but remained trapped in the microstructure and in smaller amounts. From the EDS analysis (Fig. 4c), the components presented a percentage that came reasonably close to the compositional values. The second peak in Fig. 4c is represented by the carbon detected due to the resin used to embed samples.

In this case, Sn presents 4% more content than that added. This characteristic may be due to this element's low homogeneity in the regions presented by the map (in green). However, the MA process generally promoted good microstructure homogeneity during the applied milling time.

The XRD profile of materials sintered by ERS at an electrical current density of 11, 12 and 13 kA are shown in Fig. 5. They were compared to the XRD profile powders after MA on the same scale. The XRD patterns were formed by peaks related to the α' martensite and β phases in all the samples. α' presented a smaller elastic modulus than the hexagonal α phase [41], which is interesting for orthopedic applications, but could significantly reduce mechanical strength. In Fig. 5a, the typical microstructure obtained by

Fig. 4 **a** SEM-backscattered electrons image of the cross section of powders after the 72-h milling process. **b** The micrograph merge of the Ti, Nb and Sn maps. **c** The SEM-EDS analysis of the milled powders after 72 h



the EBSD evaluation denotes the slight presence of Ti- α (represented in blue), which could not be identified by XRD.

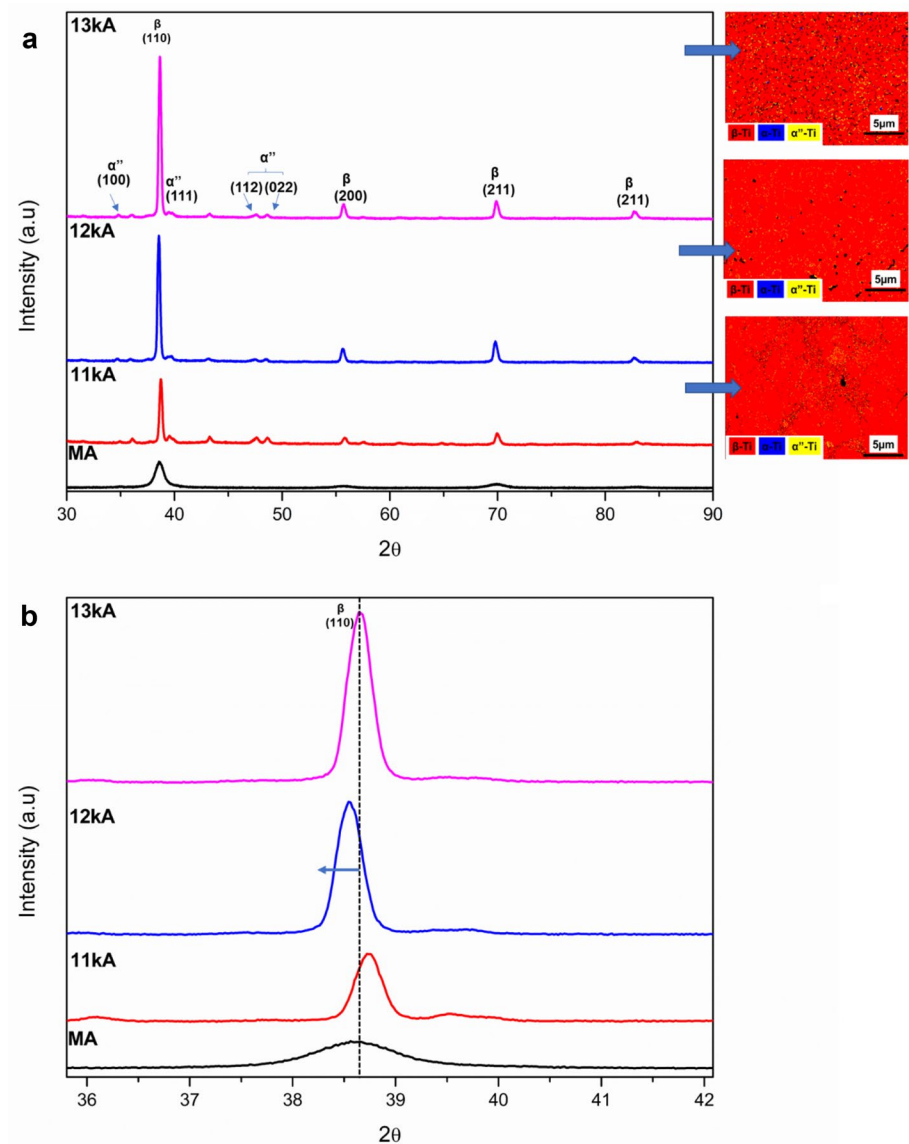
Among the alloy's component elements, Nb was present in a higher proportion compared to Sn. Nb had a higher melting point (2468 °C) than Sn (231.97 °C) and, thus, the diffusion rate was lower compared to Sn. Due to the low diffusion rate, homogeneity was also smaller and created areas rich in Ti which, in turn, became the α'' phase during the sintering process via ERS. Obtaining samples with an electrical current density at 11 kA promoted greater α'' phase formation, where peaks were more intense (Fig. 5a). This fact proved the resistance of Nb as a refractory element in the Ti matrix, accompanied by low system energy for the applied electrical current. The system's energy was lower than 12 kA and 13 kA to ensure sufficient diffusion and, thus, promoted α'' phase formation, as evidenced by the higher peak intensity. When increasing the electrical current intensity, the peaks related to the α'' phase decreased. Greater β phase stabilization could cause the transformation into β' instead of α'' . However, the presence of the ω phase, by its nanometric size, would have to be observed in TEM because it cannot be observed in XRD. No significant differences were found when comparing the XRD profile of the samples at 12 kA and 13 kA. A difference appeared between the patterns of samples obtained by ERS and powders after the A process. The main differences from powders' XRD pattern were the unique presence of the phase β , as well as mostly Ti- β and the possible Nb particles that presented the lattice parameters close to Ti- β , which made it difficult to distinguish them. However, there were no Nb particles

in powders' microstructure which, thus, discarded the presence of this undissolved element. Another significant difference was the widening of the Ti- β phase peaks related to the (110), (200) and (211) planes present in powders' XRD profile. The larger peaks and their electrical lower intensities were due to the applied milling time, the good refinement of the Nb grains and the micro-deformation inside these grains [42]. According to Fecht, grain refinement and micro-deformation increase during the milling process [43]. Besides, particles are increasingly refined when the milling time is prolonged. In the work of Zhang et al., 2018, the effect of milling Nb, Ti and silicon powders was evaluated at 2, 5, 10, 20 and 40 h. After 20 h, peaks became wider and less intense [44]. The similar results in Fig. 4 can be confirmed by the wider and less intense peaks of the milled powders compared to the sintered samples.

Mechanical milling performed for significantly long times increased beyond the local deformations in the shear strips with high displacement densities at the beginning of the refinement process. Grains are created when combining these displacements to one another, which limits low angle formation [45]. These slight limits of the formed grains were transformed into grain limits at a higher angle to produce more refinement particles. In addition, micro-deformation increased while pressing balls during MA, along with particles, and continuously collided, while irreversible deformations increased and led to micro-deformation.

Figure 5b shows more details of the largest widening β phase peak, represented by the (110) plane in the powder pattern. The increase in the employed electrical current

Fig. 5 Structural study in the central zone of samples. **a** The XRD pattern of powders after 72 h of MA and the EBSD contrast phase micrographs in samples' central zone; **b** Bragg reflections. Profiles of the peak of the β phase represented by the (110) plane of the milled Ti-34Nb-6Sn sintered at 11, 12 and 13 kA by ERS



density narrowed the widening peak, while peak intensity increased. The main reason for peak widening was the accumulation of the defects in the lattice that were produced during the milling process [46], such as displacements and point defects, which promoted the vacant site formation in the crystalline lattice or the compression of an atom present at an interstitial site in the crystalline lattice. Figure 4b also shows a displacement of the sample peaks at 11 kA and 13 kA at intenser angles. The peak related to the sample prepared at 12 kA promoted displacement at lower angles.

This effect can be explained by variation in the distances d from the plane of the crystallographic lattice. For values of $(2\theta)_{\text{final}} < (2\theta)_{\text{initial}}$, which correspond to the peak related to the sample obtained at 12 kA ($2\theta \cong 38.5$), the d values rose during sintering according to the Bragg equation

$$(2d\sin(\theta) = \lambda n) \quad (4)$$

Table 4 depicts the obtained parameters of the linear fit of powders after the 72-h milling time and the samples sintered by ERS. Figure 6a-d show the best fitted linear plots between the milled powders and the samples sintered at 11, 12 and 13 kA, respectively. Crystallites size (D) was calculated from the intercept cut on the y-axis (represented by $\beta\cos\theta$), while the lattice strain (ϵ) was determined by the slope of the fitted straight line with the Williamson-Hall equation [37]. In order to compare the evolution of crystallite size and residual stresses after material consolidation by ERS, the average grain size was estimated with the half height width of the Ti (110) $_{\beta}$ plane peak and the Scherrer equation [47].

Table 4 Parameters obtained from the multiple peaks fit analysis

Samples	FWHM = β	Height
Powders obtained by MA	1.11	2438
	1.51	126
	1.68	321
11kA	0.46	613
	0.42	517
	0.36	490
12kA	0.29	12,856
	0.36	1252
	0.40	1966
13kA	0.42	1413
	0.44	1711
	0.50	690

$$L = \frac{k\lambda}{\text{FWHM} \cos(\theta)} \quad (5)$$

where k is the shape factor (0.8–1.2), λ is the X-ray wavelength, FWHM is the full width at half maximum (in radians) and θ is Bragg's angle.

The level of deformation undergone by the lattice was evaluated after analyzing the corresponding crystallite size and residual micro-strains, as indicated in Table 5. In the present study, crystallite size increased significantly after the consolidation process of the Ti-34Nb-6Sn alloy compared to the initial value obtained during MA. The dominating deformation mechanism during the ball-milling process was the formation of shear bands, with marked dislocations density due to the constant impact associated with the powder particles on balls, as already discussed. After the long milling time, sub-grain fragmentation occurred from the region where the unstrained shear band was present in the previous material. Due to grain cracking, the degree of randomness

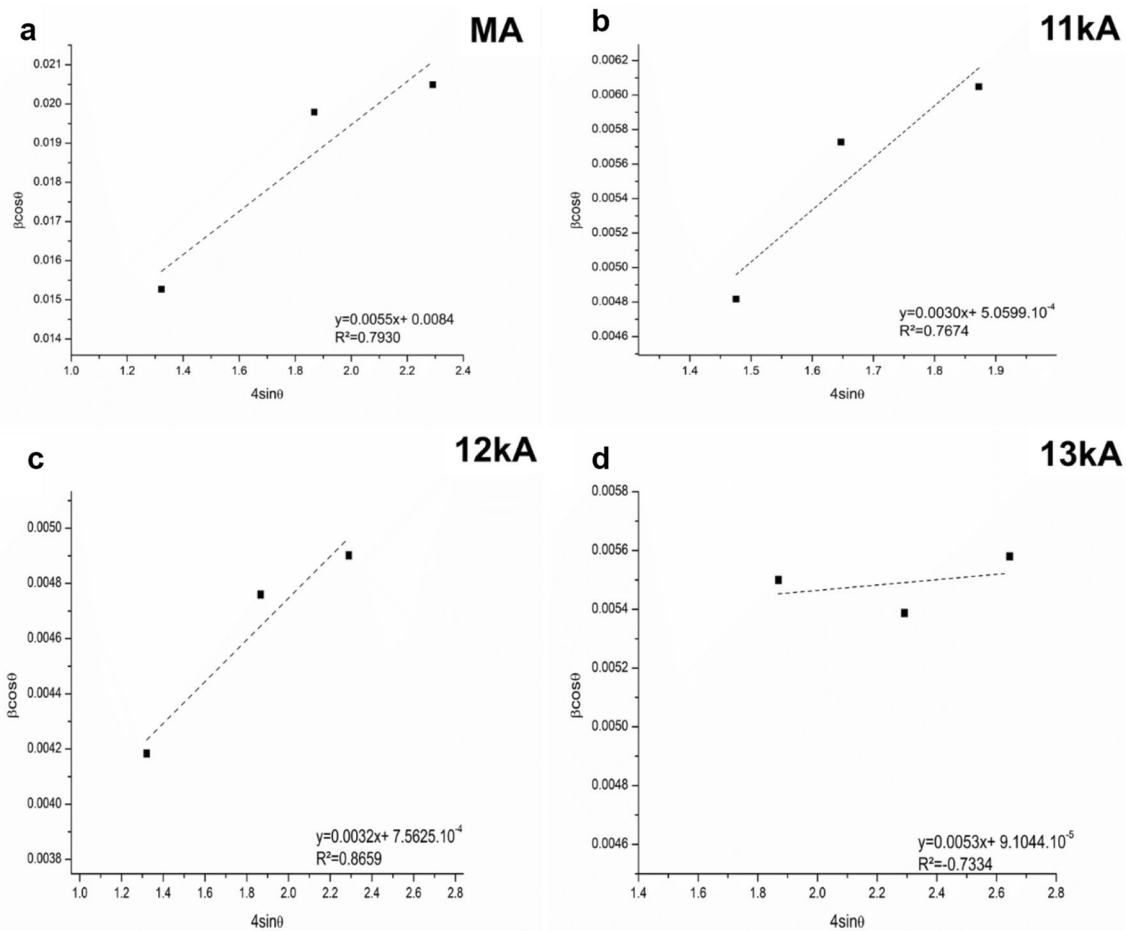


Fig. 6 Linear fit plot for the milling and sintering of the Ti₃₄Nb-6Sn alloy. **a** Linear fit plot of the powders milled for 72 h; **b** linear fit plot of the Ti-34Nb-6Sn consolidated by ERS at 11 kA; **c** Linear fit plot of

Ti-34Nb-6Sn consolidated by ERS at 12 kA; **d** linear fit of Ti-34Nb-6Sn consolidated by ERS at 13kA

Table 5 Variation in the crystallite size (D) and lattice strain (ϵ) for the Ti-34Nb-6Sn milled powders and the sintered samples by ERS

Samples	ϵ (% Strain)	D (crystallite size, nm)
Powders obtained by MA	5.5	16.51
11kA	3.0	274.02
12kA	3.2	183.40
13kA	5.3	152.37

of sub-grain orientation increased. Grain size reduction occurred until the complete random orientation of the obtained sub-grains was accomplished [48], as confirmed by the results in Tables 1, 2, 3, 4 and 5. Besides, the results obtained from parameters ϵ and D confirmed the widening and small peak intensities of the powder XRD profile, as discussed above. The diffusion of elements in the solid state is responsible for phase development. Both Nb and Sn were dissolved in Ti to form a supersaturated solid solution. As the mechanical milling of the pure Nb, Sn and Ti powders only led to peak widening, peak shifting can be ascribed to a drop in the lattice parameter of Ti owing to the diffusion of Nb and Sn, which would help the solid solution to develop. This meant that significant solid solubility was achieved only by a mechanical alloying process and all the peaks' intensity decreased compared to the sintered ones. This phenomenon occurred because of the increased strain imputed in the powder particles' structure. The average grain size substantially reduced from 51.08 μm (precursor powders) to 19.12 μm (milled powders). The particle size influence decreased on the crystallite size, as confirmed by the results indicated in Table 5, where the crystallite size after the MA process was significantly small compared to the sintered ones.

The sintering temperature evidently contributed to the significant increase in crystallite size under all the conditions. For the lower electrical current density (11 kA) condition, there is evidence for it promoting more defects in the microstructure [49] as the crystallite size is significantly bigger for this condition, which decreased with increasing electrical current density. Likewise, the samples sintered at 11 kA and 12 kA showed a decreasing trend in the lattice strain compared to the milled powders sample. However at an electrical current density of 13 kA, the value once again rose and came close to that obtained after the milling process. There was a high level of material transfer and the diffusion process was more accelerated by being induced by the higher electrical current density applied upon consolidation than the others. In this way, the creation of plasma between particles could contribute to the material's fast consolidation, along with the Joule effect and plastic deformation as a result of the compaction in the ERS technique. According to Singh et al., 2018, a high concentration of defects

occurs during the densification of samples by rapid heating, associated with rapid particle deformation [50]. This defect formation is assisted by the employed high electrical current, which is essential for generating heat. Kim et al., 2014 and Besson and Abouaf found that this defect, which is induced by deformation, was responsible for dynamic grain growth [51, 52].

Some researchers have reported that at a higher heating rate, the diffusion process of grain contours is driven by substantial stresses (inversely proportional to the pore curvature radius) because diffusion on the surface does not last long enough to "smooth" pore surfaces [53]. Pore size significantly decreases at the same time due to densification, which prevents them from exerting the fixation effect. For grain growth to occur, the sintering time must be long enough than this critical point. For high heating rates, however, grain growth slows down due to shorter processing times. In the present work, the heating time was constant and only the current density was varied. However, densification and diffusion mechanisms are the same because, with an increasing electrical current density, the system's energy increases and, consequently, heating temperature rises. Thus even at the high temperature provided by the increased electrical current density, the time was not long enough to promote a bigger crystal size, but promoted a 17% decrease.

The powders prepared by MA after 72 h were consolidated by ERS. During the first sintering, an electric current density of 11 kA was applied, as represented by Fig. 7a-c. The current promoted an advance in alloy consolidation. In the peripheral region, the material was poorly sintered, as confirmed by the presence of microporosities in the microstructure (Fig. 7a). In these regions, heat distribution was less because the presence of the zone enriched by the solute (Nb), which was not only diffused in the Ti matrix, was still noticeable (Fig. 7b). By the line analysis (Fig. 7c), lack of uniformity in the material's peripheral region was confirmed. The Sn element seemed well-dissolved in the Ti matrix due to its curve presenting linearity. Nb intensity abruptly increased upon entering the brightest contrast regions. This abrupt transition between elements indicated their transient diffusion, some of which approximately reached 2.5 μm as a result of lack of heat obtained by the system.

Figure 8a shows the low sintering process in the peripheral region persisting at 12 kA (Fig. 8b) due to the presence of not only microporosities, but also of zones enriched by the solute. However, the material's uniformity improved, with fewer regions in which particles remained completely unreacted. When looking at the places in the material's center (Fig. 8c), practically no solute particles were found, which indicates that heat distribution was more efficient for alloy consolidation.

As in Figs. 7 and 8, Fig. 9a-c indicate that the 13 kA electrical current also promoted microporosity, possibly due to

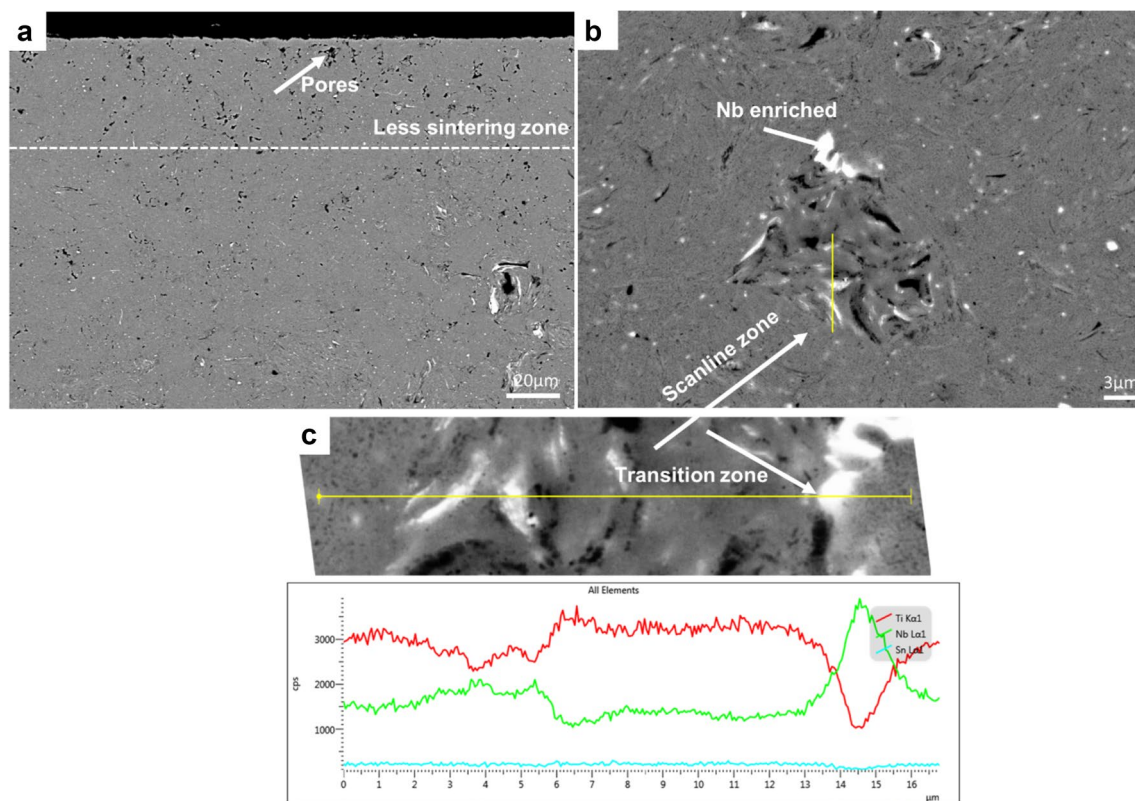


Fig. 7 SEM-backscattered electrons images of the Ti-34Nb-6Sn consolidated by ERS at 11 kA. **a** Image of the peripheral region indicating slight sintering; **b** details obtained from a poorly sintered area; **c** analysis by the scanline of the poorly sintered region

slight sintering in more distant regions from the material's central zone (Fig. 9a-b) compared to the other two conditions. In the central zone, as in other cases, practically all the material melted (Fig. 9c). Nano-pores were present in the central zone (more melted region). The marked presence of nano-pores is related and resulted from the fusion and blocking of the gas escape during solidification by sealing the surface, caused by increased electrical current density.

Orientation maps were colored in color scales from variations in the RGB (red, green and blue) scale, in relation to the z-axis, then analyzed using Inverse Pole Figures (IPFs) and Pole Figures (PFs) images. Figure 10 IPFs maps, shown color codes related to specific orientations: red, green and blue representing the family of planes $\{101\}$, $\{111\}$ and $\{001\}$, (only the β phase indexed), respectively, parallel to the x-y surface.

Density distributions were expressed as multiple unit density (MUD) with each section having a specific scale. The IPF-Z maps showed a gradual decrease in MUD from the plane (101). For grains (001) the value increased under all conditions. However, the grains (111) varied the MUD intensities, from 1.46 (maximum value), in samples obtained at 11kA, going to minimum values of 0.42 and increasing again.

The EBSD images in Fig. 11a-c represent the distribution of the grains that formed after Ti-34Nb-6Sn alloy consolidation by ERS of the central regions. Images were obtained by the cross section of the metallographically prepared materials. In Fig. 11a, the consolidated alloy with an electrical current intensity of 11 kA presents a microstructure with colonies of equiaxial bcc- β grains of a solid Ti solution (Nb, Sn) with an equivalent circle diameter (ECD) of $0.75 \mu\text{m} \pm 0.36 \mu\text{m}$. Grains also displays good homogeneity, appear to be fine and uniform, surrounding high angle boundaries ($\theta > 15^\circ$) and large number of sub-grains separating each other by low angle boundaries ($\theta < 15^\circ$) in their interior also can be seen. By increasing the electrical current intensity to 12 kA, the predominance of β grains was once again noted, with an ECD of $1.01 \mu\text{m} \pm 0.55 \mu\text{m}$ (Fig. 9b). The 12 kA intensity promoted both grain growth and decreased size homogeneity and grow up to reach nearly spherical shape. The proportion of well-defined equiaxed grains increased, along with an increase of the average grain size as compared to the first one. This effect agrees with the data obtained by Kim et al., 2014, and by Besson and Abouaf, about dynamic grain growth, as discussed above. The grains morphology in Fig. 11a and b basically differs in terms of the size of

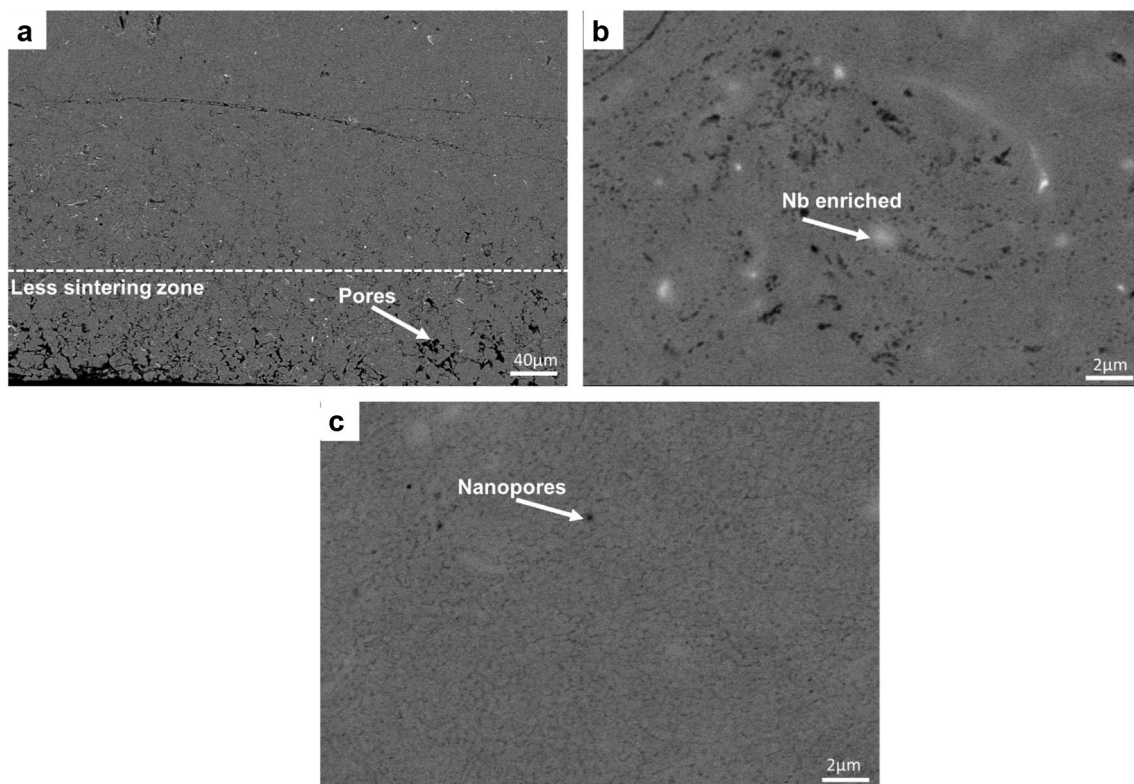


Fig. 8 SEM-backscattered electrons images of the Ti-34Nb-6Sn consolidated by ERS at 12 kA. **a** Image of the peripheral region indicating slight sintering; **b** details obtained from an intermediate zone

between the peripheral and central regions; **c** details obtained from the central region

the formed colonies. Figure 11c indicates the microstructure of the material sintered at 13 kA with a significant variation in the size of β grains due to the presence of two populations of β phase grains dispersed in the volume of the sample. The first one consists in fine grains with an average grain size of around 10 μm , and it constitutes the “shell” of the harmonic structure. The other one is made of coarse grains and a maximum of about 166 μm with an ECD of $28.14 \pm 26.86 \mu\text{m}$. These coarse grains are formed in the core of the powder particles, where no plastic deformation was produced by the thermally activated process stage. It constitutes the “core” of the harmonic structure. The presence of fine β grains is clearly observed on the close-up views of figure outlined by a black dotted line. The shell region may also be separated into the outer-consisted of micron-wide β grains and inner shell consisted of grains of nanometers wide. This difference in both microstructure size and homogeneity is associated with grain growth by the high available energy, ensured by the current density. It is clear that the microstructure became less uniform when increasing the electrical current intensity to 13 kA. However, recent works reported, the harmonic-structured materials may exhibit high work hardening that extends to higher strain regions, leading to

delay in the initiation of plastic instability. Consequently, a good combination of high strength and high ductility can be achieved [54, 55].

The microstructures developed in the first and second consolidation were formed by dynamic equilibrium sub-grain structures. Furthermore, a distinct feature of the first two microstructures compared to the third one is the formation of significant deformation/orientation gradients, which delimited the strain bands, caused by high temperatures. This implies that along with the thermally activated process, during electrical resistance sintering, some athermic processes mechanically induced by the heat available in the system can play an important role in structural changes during high temperatures. Increasing current density, the strain of the net and grains increased, providing fragmentation and refinement of the grain structure in the alloy.

To study and compare the textures of the three different processing parameters employed, the orientation density from the crystal planes of β phase was also presented in the form of pole figures (Fig. 12a-c). As the same way in IPF-Z maps, the intensities were visualized in terms of contours and colors and expressed as MUD. There was a difference in color contours in the pole figures of (100), (110) and (111) planes. The maximum MUD value increased gradually

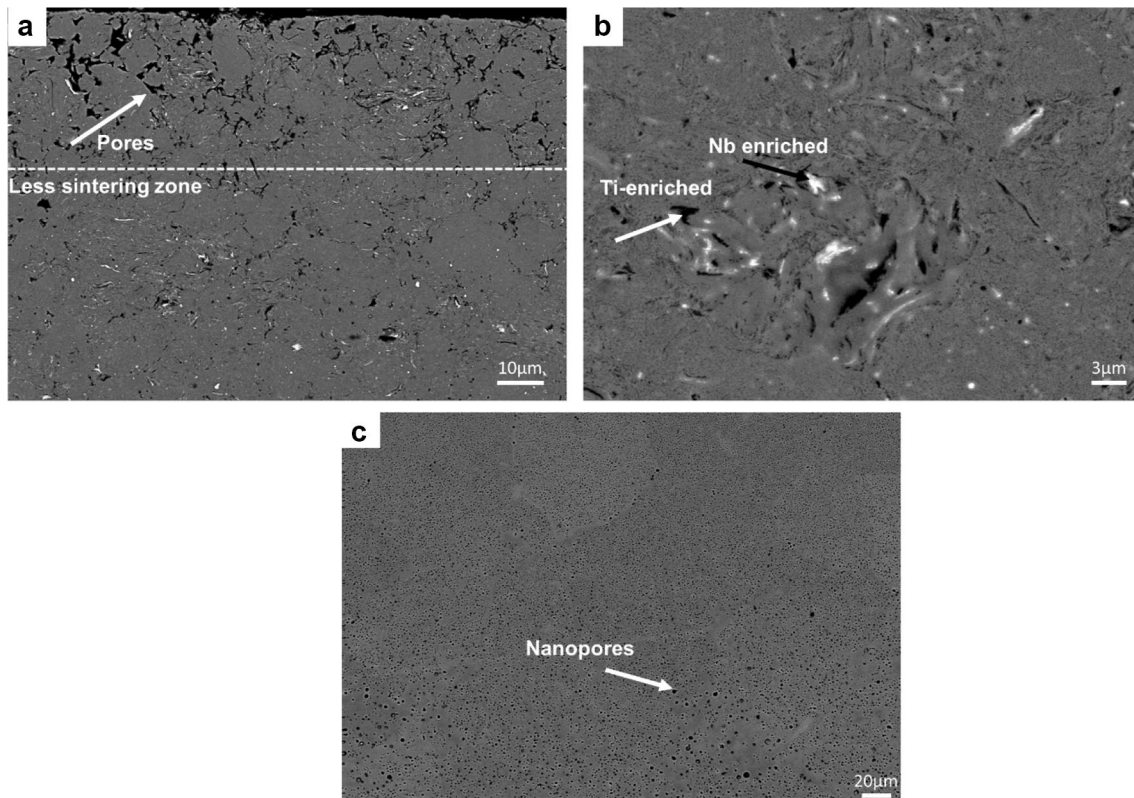


Fig. 9 SEM-backscattered electrons images of the Ti-34Nb-6Sn consolidated by ERS at 13 kA. **a** Image of the peripheral region indicating slight sintering; **b** details obtained from an intermediate zone

between the peripheral and central regions; **c** details obtained from the central region

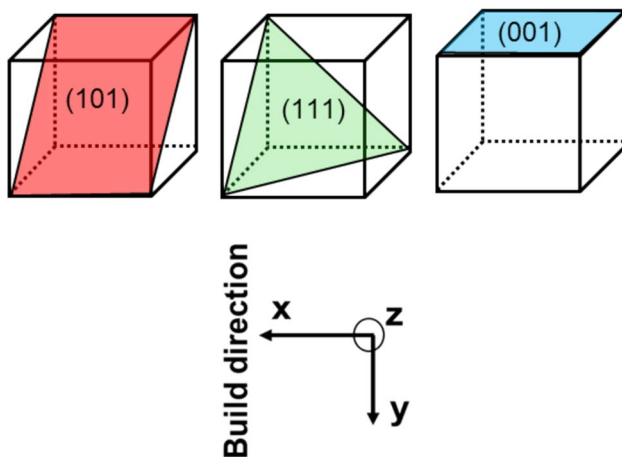


Fig. 10 β -bcc planes and their depiction in IPF key

with the increase of process parameter. There some concentrations in the (100) plane for all three samples, but more evident for (100) plane for the sample obtained at 13kA (Fig. 12c).

The concentration of the MUD value in specific locations planes indicates that there was a more significant grain

rotation, caused by the thermally activated process in a short period of time (700 ms).

Deformation of a polycrystal occurs when an external stress is supplied to the polycrystalline system, and it is transmitted to individual grains, causing “hardening”, change their shape and orientation (as discussed based on Fig. 11), thereby interacting with neighbors and creating local stress that need to be accommodate [56]. Metals under bcc structure have 12 variants of slipping system [56] and the most common deformation mode is $\{110\} \langle 111 \rangle$ slip, which is a transposition of slip plane and slip direction. Also, bcc metals slip on other planes than $\{110\}$ in the $\langle 111 \rangle$ direction [57] such as $\{112\} \langle 111 \rangle$ and $\{123\} \langle 111 \rangle$ [58]. Generally, the most preferred orientations in cold rolled bcc metals consists of two types. The first one is represented by $\{100\} \langle 110 \rangle$ or its rotations around $\langle 110 \rangle$ axis, resulting in $\{hkl\} \langle 110 \rangle$. The other is represented by $\{111\} \langle 112 \rangle$ or its orientations around surface normal axis, resulting in $\{hkl\} \langle uvw \rangle$ [58].

Table 6 indicates the phase contents obtained by the EBSD analysis with predominant β phase formation above 95% for all the conditions. During sintering at 11 kA, the β phase percentage was lower than at 12 kA and 13 kA. Under this condition, there were more pixels without

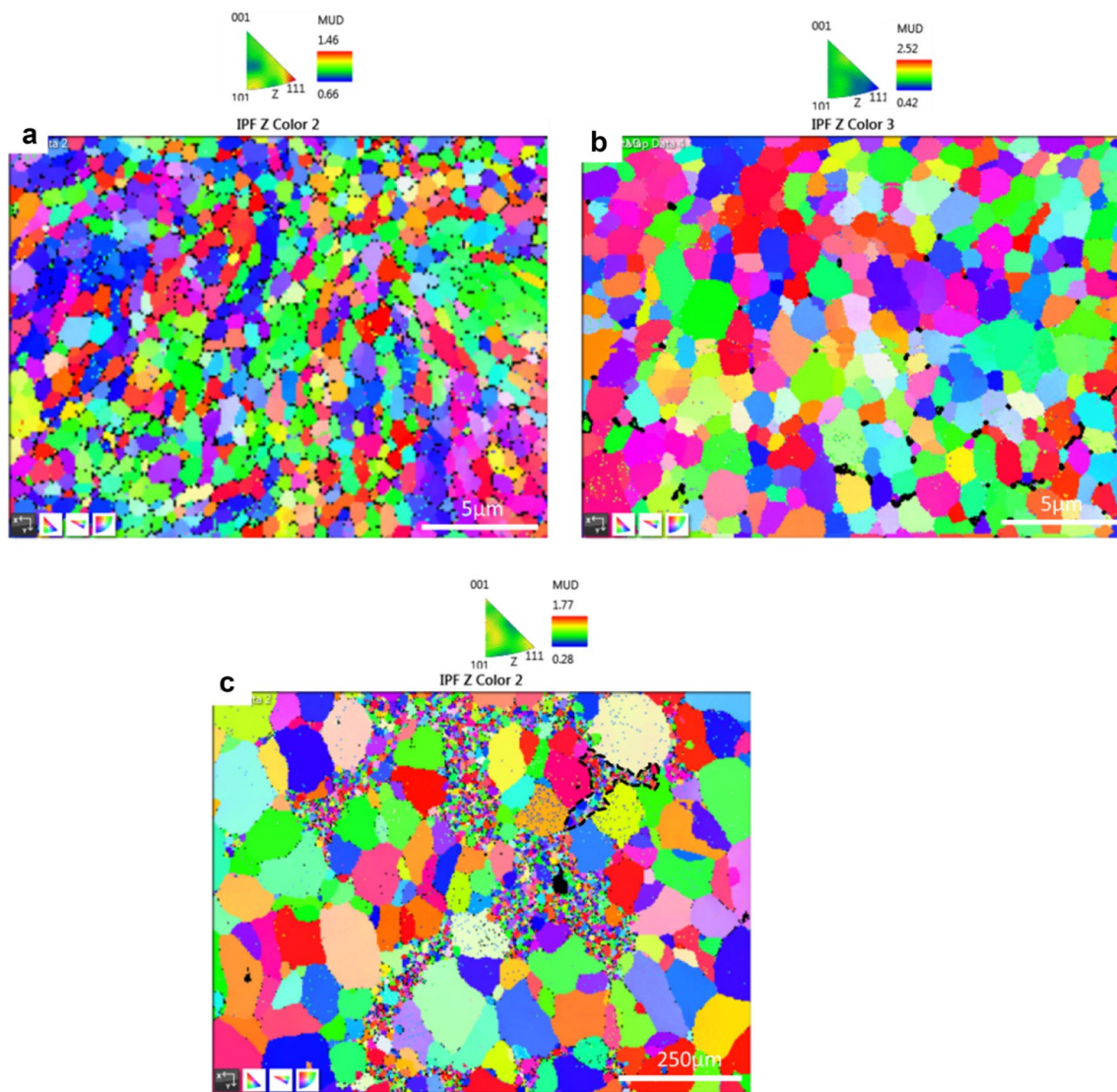


Fig. 11 EBSD IPF-Z maps for the Ti-34Nb-6Sn consolidated by ERS at: **a** 11 kA, **b** 12 kA and **c** 13 kA. Standard stereographic triangles show color-coded schematic grain orientation dependence on different planes

indexing, as evidenced by the decrease in the small amount of the α phase, as determined by the smaller amount of residual Ti. For the β phase at 12 kA, a 1.6% increase occurred in relation to the lower employed electrical current intensity. The β phase at 13 kA was higher (around 5%) compared to the samples obtained at 11 kA. The β phase content also confirmed the microstructure shown in Fig. 9, which was predominantly formed by bcc- β equiaxed grains. It is also noted that by increasing the electrical current intensity, the α'' martensite phase decreased, as did the α -Ti phase. In recent years, Sn has been classified as a neutral alloying element for Ti and its alloys. [59, 60]. As such, it has no significant impact on α or β phase stability, but contributes to the formation of solid solutions with Ti [61, 62]. Moreover, the presence of Sn

in Ti alloys can limit the presence of the martensite phase, which is unfavorable in Ti alloys. The scarce presence of these phases after the sintering process can be related to this factor. In more detail, the solid solution forms when solute atoms (e.g., Sn) are added to the host material (Ti). Then, the crystal structure is maintained and no other structure forms [63, 64]. After the sintering process, the patterns related to these samples shown in Fig. 4 contain two formed phases: α'' and β . The α'' martensite phase formed in the three samples under different processing conditions (11 kA, 12 kA, 13 kA) and showed no significant difference in the formed content. Some authors have demonstrated that the initial martensite transformation temperature (M_s) for contents of 2–9 Sn wt% falls within the 740–760°C range independently of alloy composition

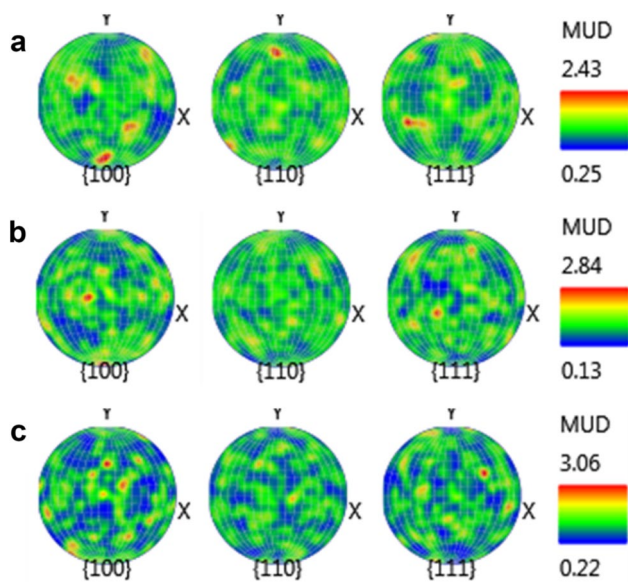


Fig. 12 PFs of the grains obtained after consolidation by ERS at a 11kA, 12kA and c 13kA

Table 6 Percentage of phases analyzed by EBSD at the different sintering current intensities after Ti-34Nb-6Sn consolidation by ERS

Intensity current (kA)	Phase name	Phase fraction (%)	Phase count
11	Titanium cubic	96.56	36,127
	Ti-Hex	0.27	101
	Ti-alpha 2 prima	3.17	1187
12	Titanium cubic	98.12	153,313
	Ti-Hex	0.09	144
	Ti-alpha 2 prima	1.79	2792
13	Titanium cubic	98.02	105,540
	Ti-Hex	0.03	38
	Ti-alpha 2 prima	1.95	2105

[65]. This, and the similarity between the atomic radii of Sn and Ti (difference < 15%), can explain a low content of the formed martensite phase being present. Besides, the insignificant differences between the peaks related to this phase demonstrate its excellent efficiency as a neutral element. As studied by Gouvea et al., 2019, the same growth trend of β grains was observed by increasing the electric current from 14 to 16 kA and, hence, to the bimodal distribution of grains at a higher current intensity (16 kA) [66]. In our case, the process also occurred at a higher electrical current (13 kA), but at a lower than that used, to produce samples with a 16 mm diameter that compressed at 50 MPa. The possibility of increasing grain size early could be due to the lower content of the employed β phase stabilizer element, and also to the longer milling time. In

the work by Gouvea et al., 2019, both refractory elements Nb and Mo were used as β phase stabilizers.

Microhardness was measured on samples' surface regions to obtain more reliable results under different conditions. Given the greater microstructure homogeneity of the samples' central zone by ERS, measures were also taken in this region. According to Table 7, microhardness decreased with increasing electrical current intensity, where the α'' phase content lowered and grain growth formed. In the work of Amigó-Mata et al., 2019, the Ti-6Al-4 V and Ti-CP consolidated by ERS at 10 kA and 12 kA were studied. The materials presented a slightly decreased microhardness at increasing current intensities [67]. Decreased hardness could be related to materials' rapid sintering, which reduces oxidation. The work of Li et al., 2019, studied as-cast Ti-Nb-Sn alloys with different compositions. Hardness values ranged from 346.7 HV-265 HV [31], which are lower than those in the present study. Besides, the above authors found that the α'' martensite phase affected alloys' Vickers hardness because, when the α'' martensite phase content lowered, alloys' Vickers hardness reduced, which confirms the same results obtained in the present work. In the work of Utomo et al., 2018, the influence of the element Sn on the Ti-Nb-Sn system's microhardness was studied. Alloys Ti-30Nb-2Sn, Ti-30Nb-5Sn and Ti-30Nb-8Sn had hardness values of 473, 455 and 559 HV (as-cast), respectively [68]. Hardness values were higher in all cases than those herein found. The hardness value depends on several factors, such as alloy composition, oxygen content, microstructure or surface conditions, and also on the type of processing used to obtain samples. Compared to alloys Ti-CP and Ti-6Al-4 V with hardness values of around 200 HV and 340 HV [69], the obtained values were much higher.

Figure 13a-b shows the OCPs *versus* the time curves of the samples sintered at 11, 12 and 13 kA in Ringer Hartmann's solution at 37°C. The curves of each material after immediate immersion in solution (close to 5 min) rapidly increased the potential at noble potential values (Fig. 13a), which evidenced the growth of a protective passive film. Figure 13b shows the details of the OCP values during the last 10 min. The sample obtained under the 11 kA condition presented a stable OCP at -0.06 V, which remained stable throughout the experimental time. Under the 12 kA condition, curves showed a more noble potential than 11 kA, with

Table 7 Microhardness of the Ti-34Nb-6Sn alloy after consolidation by ERS

Condition	Microhardness (HV)
11kA	418.65 ± 18.82
12kA	404.25 ± 26.06
13kA	389.25 ± 21.53

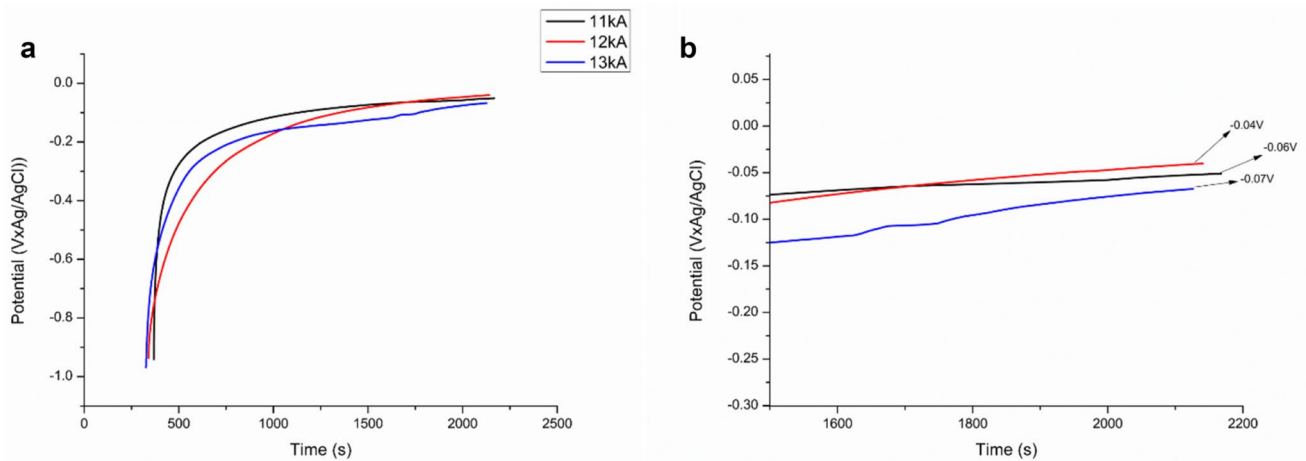


Fig. 13 **a** The OCP curves of the Ti-34Nb-6Sn alloy obtained by the potentiodynamic test carried out under different experimental conditions obtained by ERS; **b** indication of the stability zones on the OCP curves referred to in Figure a

a value of -0.04 V, and also under the 11 kA condition, and remained constant during the analysis time. The 13 kA condition had the lowest OCP, which took a value of -0.08 V.

Potentiodynamic polarization curves (PPCs) (see Fig. 14) showed that the samples obtained at 11 kA and 12 kA exhibited lower corrosion current density (i_{corr}) and higher corrosion potentials (E_{corr}). Figure 14 also depicts the regions characterized by an almost constant current density, as indicated between the dashed lines. The oxidation rate lowered due to a protection effect of the passive layer that formed on the sample surfaces in the active state. The passive layer grew while polarizing materials until a further increase in current intensity was observed, which indicated that the transpassive process had started. This increased current in the transpassive region was related to oxygen evolution, the electrode and/or fitting corrosion, intense oxidation and dissolution in the isolated points on the unshielded passive metal surface. The estimated corrosion potential (E_{corr}) of the curves for the alloy sintered at 11 kA was $-0.43 \text{ V} \pm 0.13 \text{ V}$, $-0.40 \text{ V} \pm 0.09 \text{ V}$ at 12 kA and $-0.47 \text{ V} \pm 0.015 \text{ v}$ at 13 kA. As found on the OCP curves, E_{corr} showed the same tendency to not only increase given a rise in the sintering electrical current density at 12 kA, but to decrease with an increase at 13kA, which promoted less uniformity in grain size and the more abounding presence of porosity. Afonso et al., 2020, demonstrated the correlation between hardness, E_{corr} , and the Nb content of solidified Nb-Ni binary systems [70]. It was evidenced that hardness and E_{corr} were inversely proportional parameters. This fact was herein observed as hardness decreased when the current intensity increased from 11 to 12 kA and the E_{corr} value increased. However, for the sample obtained at 13 kA, the hardness value was lower than that obtained at 11 kA and 12 kA, but

Table 8 Kinetic parameters obtained from the anodic curves by the potentiodynamic test

Condition	i_{corr} ($\mu\text{A}/\text{cm}^2$)	E_{corr} (V)	R_p (K Ω)	C_r ($\mu\text{m}/\text{year}$)
11kA	0.38 ± 0.25	-0.43 ± 0.13	84.4 ± 55.63	2.67
12kA	0.45 ± 0.06	-0.40 ± 0.09	56.2 ± 8.21	3.16
13kA	0.24 ± 0.01	-0.47 ± 0.15	111 ± 29.44	1.68

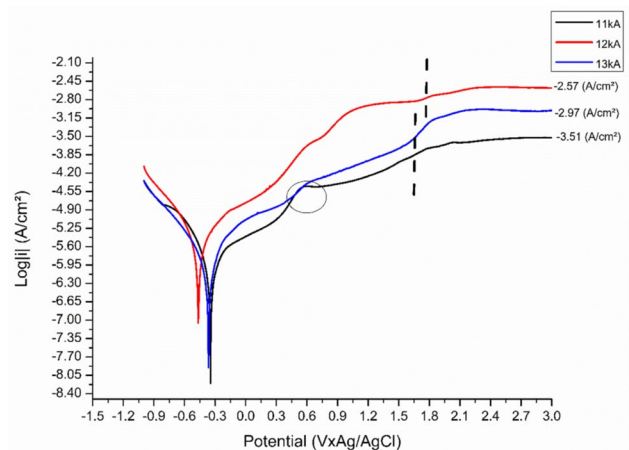


Fig. 14 The PPC curves of the Ti-34Nb-6Sn alloy obtained by the potentiodynamic test carried out under the different experimental conditions obtained by ERS

E_{corr} significantly decreased. This fact can be attributed to microstructure non uniformity as confirmed by the previously discussed grain size heterogeneity.

These potentials obtained (Table 8) by polarization curves were significantly lower than those acquired by OCP measurements because the polarization test began at a cathodic

potential. In this way, the passive oxide film on the surface was partially removed due to cathodic polarization.

Polarization resistance followed the same tendency as the E_{corr} values considered for 11 kA and 12 kA, which led to a lower R_p . R_p significantly increased under the 13 kA condition. This increase could be explained for a longer time because microstructural homogeneity was lacking. Figure 14 shows the regions characterized by an almost constant current density, starting where the dashed lines indicate. This region indicates the formation and growth of a passive film on samples' surfaces. Under the 11 kA and 13 kA conditions, the passivation process started at a potential close to 1.7 V. For the material obtained at 12 kA, the start of passivation came close to 1.8 V, which demonstrated later passivation. This can be confirmed by the corrosion resistance parameter, C_r , obtained by using the i_{corr} of each sample (see Table 8).

In the work of Mavros et al., [71], the Ti-Nb-Zr-Ta alloy system was obtained for biomedical application by the SPS technique with good corrosion resistance. The excellent corrosion resistance of the β -type alloys formed by refractory elements, such as Nb, can contribute to the formation of a passive film layer that was not released to the environment [71]. In addition, both this oxide layer formed on the surface of Ti alloys and its composition affect these alloys' corrosion response when used to manufacture orthopedic prostheses [6].

The corrosion current density found for this alloy type fell within the 0.4 to 0.7 $\mu\text{A}/\text{cm}^2$ range. It is worth mentioning that the employed solution was NaCl, which has an ionic concentration and a different pH from those present in body fluid (Ringer Hartmann's solution). The Ti-Nb-Zr system, which was also obtained by SPS, had a much higher corrosion current density value than in the present work, with 2.42 $\mu\text{A}/\text{cm}^2$ for the Ti-13Nb-13Zr alloy. For the commercially pure Ti, one of the most widely used materials in the biomedical sector, I_{corr} was approximately 3 $\mu\text{A}/\text{cm}^2$ [72], which was significantly higher than the values found for the Ti-34Nb-6Sn alloy for all conditions included in the present work.

Figure 15 indicates the Nyquist diagrams of the EIS experiments in the samples sintered at 11, 12 and 13 kA. For the obtained EIS, data were modeled on the basis of the CPE circuit shown in the inset of Fig. 15. The best fitting (goodness of fit, see Table 9) was provided using the equivalent circuit of R_s (CPEdl R_{ct}) for all the samples. In the equivalent circuit, R_s and R_{ct} referred to solution resistance and circuit resistance, respectively. Another variable employed to describe passive layers, ndl , is the coefficient of CPEdl, which is interphase CPEdl and the electrolyte and transfer charge resistance related to Cdl (Eq. 6). The Cdl parameter of the samples was calculated according to the following equation (see Table 9):

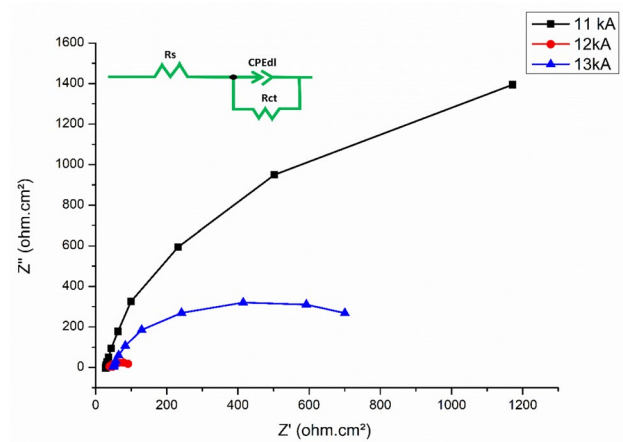


Fig. 15 The typical Nyquist diagram for the tested samples and the equivalent electric circuit for the EIS data analysis (R_s -solution resistance, R_{ct} -circuit resistance, CPEdl-constant phase element (non-ideal capacitance))

$$Cdl = \left(\frac{CPEdl}{(R_s^{-1} + R_{ct}^{-1})^{1-ndl}} \right)^{1-ndl} \quad (6)$$

The impedance spectra of three samples presented different characteristics. The first (at 11kA) showed half capacitive arc resistance characteristics. The impedance spectrum radius was larger compared to the other samples, with greater corrosion resistance. The second and third samples (at 12 kA and 13 kA) showed similar Nyquist spectra to the semicircular arc. This characteristic is present in passive metals or the capacitor [73]. Moreover, the end of the semi-circle of the plots of the second and third samples reached 700 Ω and 94 Ω on the x-axis. In the first sample, obtained at 11 kA, the half capacitive arc was 1175 Ω on the x-axis.

The R_s values of the samples obtained at 12 kA and 13 kA were similar, while these values were lower at 11 kA (%). The R_{ct} s for all the samples were higher than the R_s values. The highest value was obtained at 11 kA, followed by the sample obtained at 13 kA and finally at 12 kA. A high R_{ct} value is associated with good corrosion resistance. It has already been established that the high density of grain boundaries in metals with nano-size grains improves the production of a passive layer on the metallic surface [74], which further enhances corrosion resistance by restraining the interaction between metals in an aggressive situation. A small nano-sized grain was obtained in the samples prepared at 11 kA ($ECD = 750 \text{ nm} \pm 360 \text{ nm}$). The Ti-Nb-Sn samples obtained lower electrical current density, which suggests that some defects permit aggressive species to find solutions and to create susceptibility to corrosion on Ti. Hence, the higher R_{ct} and the lower Qdl values observed in the

Table 9 The parameters calculated from the electrochemical impedance spectroscopy (EIS) measurements

Condition	Goodness of Fit	Rs	CPEdl-T	ndlCPEdlP	Rct	Cdl($\mu\text{F}/\text{cm}^2$)
11kA	0.00334	28.95 ± 0.27	$2.28 \times 10^5 \pm 7.22 \times 10^7$	0.92 ± 0.00	3318 ± 142	11.90
12kA	0.000665	37.24 ± 0.44	$7.97 \times 10^5 \pm 1.07 \times 10^5$	0.74 ± 0.02	71.85 ± 2.43	10.23
13kA	0.00365	37.09 ± 0.51	$7.09 \times 10^5 \pm 5.43 \times 10^6$	0.73 ± 0.01	556 ± 24.73	8.29

sample produced at 13 kA denoted nobler electrochemical performance, which agrees well with the potentiodynamic polarization results.

4 Conclusions

The Ti-Nb-Sn system with 34 wt% (Nb) and 6 wt% (Sn) was obtained by the ERS process at electrical current densities of 11, 12 and 13 kA. The effect of current density on the microstructure was evaluated. The main conclusions are highlighted:

- Samples are structured in the α , α'' and β phases. When increasing electrical current density, the β phase rises to values of around 98%;
- The samples obtained at 12 kA presented good microstructure homogeneity (less micro- and nano-pores, and fewer non soluble particles present);
- The microstructure is formed by equiaxial bcc- β grains, with a more uniform grain size in the samples obtained at 11 kA and 12 kA;
- The IPFs and PFs color maps reveal that the samples consist of very weak crystallographic texture occasioned by the both plastic deformation and thermally activated process more evident in the sample obtained at 13kA;
- Microhardness decreased with increasing electrical current density with values within the 389–418 HV range;
- Corrosion tests proved alloys' excellent corrosion resistance with low current densities despite the presence of micro- and nano-pores.
- The corrosion rate was very low in all cases, but the standard deviations were much higher in the samples obtained at 13 kA in relation to lack of microstructure uniformity.

Acknowledgements The authors thank the AMES Company for the materials development.

Author contributions Conceptualization: [Mariana Correa Rossi], Methodology: [Mariana Correa Rossi], Formal analysis and research: [Mariana Correa Rossi], [Vicente Amigó Borrás]; Writing—original draft preparation: [Mariana Correa Rossi]; Writing—review and editing: [Margarida Saeki],[Vicente Amigó Borrás]; Data acquisition [Eber de Santi Gouvêa], [Montserrat Vicenta Haro Rodríguez],

[Angel Vicente Escuder] Funding acquisition: [Mariana Correa Rossi],[Vicente Amigó Borrás]; Supervision: [Vicente Amigó Borrás].

Funding This work was supported by the Fundação de Amparo à Pesquisa do Estado de São Paulo (FAPESP) [grant: 2019/24237–6]; Ministerio de Economía y Competitividad de España for the research project RTI2018-097810-B-I00 and the European Commission through FEDER.

Declarations

Conflicts of interest The authors declare that they have no known competing financial interests or personal relationships that may have appeared to influence the work reported in this paper.

References

1. N. Eliaz, Corrosion of metallic biomaterials: a review. *Mater.* **12**, 407 (2019). <https://doi.org/10.3390/ma12030407>
2. E.J. Evans, Cell damage in vitro following direct contact with fine particles of titanium, titanium alloy and cobalt-chrome-molybdenum alloy. *Biomaterials* **442**, 713–717 (1994). [https://doi.org/10.1016/0142-9612\(94\)90170-8](https://doi.org/10.1016/0142-9612(94)90170-8)
3. J.E. Bowerman, B. Conroy, A universal kit in titanium for immediate replacement of the resected mandible. *J. Oral. Surg.* **6**, 223–228 (1969). [https://doi.org/10.1016/s0007-117x\(68\)80041-1](https://doi.org/10.1016/s0007-117x(68)80041-1)
4. D.G. Barceloux, J. Toxicol. Clin. Toxicol. **37**, 265–278 (1999). <https://doi.org/10.1081/clt-100102425>
5. J.K. Marquis, Aluminum neurotoxicity: an experimental perspective. *Bull. Environ. Contam. Toxicol.* **29**, 43–49 (1982). <https://doi.org/10.1007/BF01606087>
6. M. Long, H.J. Rack, Titanium alloys in total joint replacement—a materials science perspective. *Biomaterials* **19**, 1621–1639 (1998). [https://doi.org/10.1016/S0142-9612\(97\)00146-4](https://doi.org/10.1016/S0142-9612(97)00146-4)
7. M. Niinomi, Mechanical properties of biomedical titanium alloys. *Mater. Sci. Eng. A.* **3**, 231–236 (1998). <https://doi.org/10.1016/j.actbio.2006.11.002>
8. H. Kroger, P. Venesmaa, J. Jurvelin, H. Miettinen, O. Suomalainen, E. Alhava, Bone density at the proximal femur after total hip arthroplasty. *Clin. Orthop. Relat.* **352**, 66–74 (1998)
9. T. Ozaki, H. Matsumoto, S. Watanabe, S. Hanada, Beta Ti alloys with low young's modulus. *Mater. Trans.* **45**, 2776–2779 (2004). <https://doi.org/10.2320/matertrans.45.2776>
10. I.J. Polmear, Overview: recent developments in light alloys. *Mater. Trans.* **37**, 12–31 (1996). <https://doi.org/10.2320/matertrans1989.37.12>
11. J.L. Murray, The Nb-Ti (Niobium-Titanium) system. *Phase Diagr.* **2**, 55–61 (1981)
12. L. Zhu, Q. Zhang, Z. Chen, W. Changdong, C. Ge-Mei, J. Liang, J. Zhanpeng, Z. Ji-Cheng, Measurement of interdiffusion and impurity diffusion coefficients in the bcc phase of the Ti-X (X = Cr, Hf, Mo, Nb, V, Zr) binary systems using diffusion multiples.

- J. Mater. Sci. **52**, 3255–3268 (2017). <https://doi.org/10.1007/s10853-016-0614-0>
13. B. Sharma, S.K. Vajpai, K. Ameyama, Synthesis of ternary Ti-25Nb-11Sn alloy by powder metallurgy route using titanium hydride powder. *Mater. Trans.* **57**, 1440–1446 (2016). <https://doi.org/10.2320/matertrans.mh201510>
 14. M.S. Yahaya, M. Sulaiman, N.H.N.E. Azham Shah, M.H. Ismail, Microstructures and mechanical properties of Ti-Nb alloy at different composition of Nb produced via powder metallurgy route. *Mater. Sci. Forum.* **863**, 14–18 (2016)
 15. J. Lux, Improved manufacture of electric incandescence lamp filaments from tungsten or molybdenum or an alloy thereof. GB Patent. 1906
 16. G.F. Taylor, Apparatus for Making Hard Metal Compositions. U.S. Patent 1,896,854, 7 February 1933
 17. F.V. Lenel, Resistance sintering under pressure. *J Alloy Compd.* **7**, 158–167 (1955). <https://doi.org/10.1007/BF03377473>
 18. T.L. Istomina, A.A. Baidenko, A.I. Raichenko, M.A. Goldberg, A.V. Svechikov, Influence of premolding pressure in electric-discharge sintering on the physicomechanical properties of a copper-tin-abrasive composite. *Sov. Powder Metal. Met. Ceram.* **22**, 957–960 (1983). <https://doi.org/10.1007/BF00805559>
 19. G.L. Burenkov, A.I. Raichenko, M. Suraeva, Dynamics of interparticle reactions in spherical metal powders during electric sintering. *Sov. Powder Metall. Met. Ceram.* **26**, 709–712 (1987). <https://doi.org/10.1007/BF00797175>
 20. S. Grasso, Y. Sakka, G. Maizza, Electric current activated/assisted sintering (ECAS): a review of patents 1906–2008. *Sci. Technol. Adv. Mater.* **10**, 053001 (2009)
 21. R. Orrù, R. Licheri, A.M. Locci, A. Cincotti, G. Cao, Consolidation/synthesis of materials by electric current activated/assisted sintering. *Mat. Sci. Eng. R Rep.* **63**, 127–287 (2009). <https://doi.org/10.1016/j.mser.2008.09.003>
 22. E.A. Olevsky, D.V. Dudina, *Field-Assisted Sintering Science and Applications*, first ed., Cham, Switzerland, 2018.
 23. A. Fais, A faster FAST: electro-sinter-forging. *Metal Powder Rep.* **73**, 80–86 (2018). <https://doi.org/10.1016/j.mprp.2017.06.001>
 24. E. Cannella, C.V. Nielsen, N. Bay, Process investigation and mechanical properties of electro sinter forged (ESF) titanium discs. *Int. J. Adv. Manuf. Technol.* **104**, 1985–1998 (2019). <https://doi.org/10.1007/s00170-019-03972-z>
 25. U. Anselmi-Tamburini, J.R. Groza, Critical assessment: Electrical field/current application. A revolution in materials processing/sintering. *Mater. Sci. Technol.* **33**, 1855–1862 (2017). <https://doi.org/10.1080/02670836.2017.1341692>
 26. M.C. Rossi, D.L. Bayerlein, J.S. Brandao, J.P.H. Pfeifer, G.S. Rosa, W.M. Silva, L.G. Martinez, M.J. Saeki, A.L.G. Alves, Physical and biological characterizations of TiNbSn(Mg) system produced by powder metallurgy for use as prostheses material. *J Mech. Behav. Biomed. Mater.* **115**, 104260 (2021). <https://doi.org/10.1016/j.jmbbm.2020.104260>
 27. M.C. Rossi, D.L. Bayerlein, E.S. Gouvea, V.M.R. Haro, V.A. Escuder, V.B. Amigo, Evaluation of the influence of low Mg content on the mechanical and microstructural properties of beta titanium alloy. *J. Mater. Res. Technol.* **10**, 916–925 (2021). <https://doi.org/10.1016/j.jmrt.2020.12.103>
 28. G.M.A. Mahran, A.-N.M. Omran, Fabrication of a β Ti–30Nb–4Sn biomedical alloy using mechanical alloying. *Sci. Adv. Mater.* **10**, 1509–1518 (2018). <https://doi.org/10.1166/sam.2018.3352>
 29. D.R. Adiningsih, E.P. Utomo, The microstructure and mechanical hardness of cast Ti-30Nb-5Sn after solution treatment. *IOP Conf Ser Mater Sci Eng.* **541**, 012049 (2019). <https://doi.org/10.1088/1757-899X/541/1/012049>
 30. B. Sharma, S.K. Vajpai, K. Ameyama, Synthesis of ternary Ti-25Nb-11Sn alloy by powder metallurgy route using titanium hydride powder. *Mater. Trans.* **57**, 1440–1446 (2016). <https://doi.org/10.2320/matertrans.MH201510>
 31. P. Li, X. Ma, D. Wang, H. Zhang, Microstructural and mechanical properties of β -Type Ti–Nb–Sn biomedical alloys with low elastic modulus. *Metals.* **9**, 712 (2019). <https://doi.org/10.3390/met9060712>
 32. S. Cai, L. Wang, J.E. Schaffer, J. Gao, Y. Ren, Influence of Sn on martensitic beta Ti alloys. *Mater. Sci. Eng. A.* **743**, 764–772 (2019). <https://doi.org/10.1016/j.msea.2018.11.095>
 33. H. Matsumoto, S. Watanabe, S. Hanada, Microstructures and mechanical properties of metastable β TiNbSn alloys cold rolled and heat treated. *J Alloys Compd.* **439**, 146–155 (2007). <https://doi.org/10.1016/j.jallcom.2006.08.267>
 34. M.F. Ijaz, H.Y. Kim, H. Hosoda, S. Miyazaki, Effect of Sn addition on stress hysteresis and superelastic properties of a Ti–15Nb–3Mo alloy. *Scripta Mater.* **72–73**, 29–32 (2014)
 35. M.A. Lagos, I. Agote, T. Schubert, T. Weissgaerber, J.M. Gallardo, J.M. Montes, L. Prakash, C. Andreouli, V. Oikonomou, D. Lopez, J.A. Calero, Development of electric resistance sintering process for the fabrication of hard metals: Processing microstructure and mechanical properties Abbreviations. *Int J Refract Metals Hard Mater.* **66**, 88–94 (2017). <https://doi.org/10.1016/j.ijrmhm.2017.03.005>
 36. G.K. Williamson, W.H. Hall, X-ray line broadening from filed aluminium and wolfram. *Acta Metall.* **1**, 22–31 (1953). [https://doi.org/10.1016/0001-6160\(53\)90006-6](https://doi.org/10.1016/0001-6160(53)90006-6)
 37. A.M. Soufiani, F. Karimzadeh, M. Enayati, Formation mechanism and characterization of nanostructured Ti6Al4V alloy prepared by mechanical alloying. *Mater. Des.* **37**, 152–160 (2012). <https://doi.org/10.1016/j.matdes.2011.12.044>
 38. L.M. Zou, C. Yang, Y. Long, Z.Y. Xiao, Y.Y. Li, Fabrication of biomedical Ti-35Nb-7Zr-5Ta alloys by mechanical alloying and spark plasma sintering. *Powder Metall.* **55**, 65–70 (2012). <https://doi.org/10.1179/1743290111Y.0000000021>
 39. J. Málek, F. Hnilica, J. Veselý, B. Smola, Heat treatment and mechanical properties of powder metallurgy processed Ti-35.5 Nb-57Ta beta-titanium alloy. *Mater. Charact.* **84**, 225–231 (2013). <https://doi.org/10.1016/j.matchar.2013.08.006>
 40. L. Lutterotti, S. Matthies, H.R. Wenk, MAUD: a friendly java program for material analysis using diffraction. *IUCr Newsl. CPD.* **21**, 14–15 (1999)
 41. C.M. Lee, C.P. Ju, J.H.C. Lin, Structure property relationship of cast Ti-Nb alloys. *J. Oral Rehabil.* **29**, 314–322 (2002). <https://doi.org/10.1046/j.1365-2842.2002.00825.x>
 42. C. Slama, M. Abdellaoui, Microstructure characterization of nanocrystalline (Ti0.9W0.1) C prepared by mechanical alloying. *Int. J. Refract. Met. Hard Mater.* **54**, 270–278 (2016). <https://doi.org/10.1016/j.ijrmhm.2015.07.018>
 43. H.J. Fecht, Nanostructure formation by mechanical attrition. *Nanostruct. Mater.* **6**, 33–42 (1995)
 44. L. Zhang, X. Guo, Microstructural evolution, thermal stability and microhardness of the Nb–Ti–Si-Based alloy during mechanical alloying. *J. Met.* **8**, 403 (2018). <https://doi.org/10.3390/met8060403>
 45. A.F. Mohamed, A dislocation model for the minimum grain size obtainable by milling. *Acta Mater.* **51**, 4107–4119 (2003). [https://doi.org/10.1016/s1359-6454\(03\)00230-1](https://doi.org/10.1016/s1359-6454(03)00230-1)
 46. K.V. Sanjay, A. Kei, A novel powder metallurgy processing approach to prepare fine-grained Ti rich TiAl-based alloys from pre-alloyed powders. *J. Intermet.* **42**, 146–155 (2013). <https://doi.org/10.1016/j.intermet.2013.06.006>
 47. A.L. Patterson, The scherrer formula for X-Ray particle size determination. *Phys. Rev.* **56**, 978–982 (1939). <https://doi.org/10.1103/physrev.56.978>
 48. P. Singh, A. Abhash, B.N. Yadav, M. Shafeeq, I.B. Singh, D.P. Mondal, Effect of milling time on powder characteristics and

- mechanical performance of Ti4wt%Al alloy. *Powder Technol.* **342**, 275–287 (2018). <https://doi.org/10.1016/j.powtec.2018.09.075>
49. A. Khorsand Zak, W.H. Abd Majid, M.E. Abrishami, R. Yousefi, *Solid State Sci.* **13**, 251 (2011)
 50. L.K. Singh, A. Bhadauria, S. Jana, T. Laha, Effect of sintering temperature and heating rate on crystallite size, densification behaviour and mechanical properties of Al-MWCNT nanocomposite consolidated via spark plasma sintering. *Acta Metall Sin-Engl.* **31**, 1019–1030 (2018). <https://doi.org/10.1007/s40195-018-0795-4>
 51. B.N. Kim, K. Hiraga, K. Morita, H. Yoshida, Y.J. Park, Y. Sakka, Dynamic grain growth during low-temperature spark plasma sintering of alumina. *Scr. Mater.* **80**, 29–32 (2014). <https://doi.org/10.1016/j.scriptamat.2014.02.015>
 52. J. Besson, M. Abouaf, Grain growth enhancement in alumina during hot isostatic pressing. *Acta Metall. Mater.* **39**, 2225–2234 (1991). [https://doi.org/10.1016/0956-7151\(91\)90004-K](https://doi.org/10.1016/0956-7151(91)90004-K)
 53. E.A. Olevsky, S. Kandukuri, L. Froyen, Consolidation enhancement in spark-plasma sintering: impact of high heating rates. *J. Appl. Phys.* **102**, 114913 (2007). <https://doi.org/10.1063/1.2822189>
 54. B. Sharma, K. Nagano, M. Kawabata, K. Ameyama, Microstructure and mechanical properties of hetero-designed Ti-25Nb-25Zr alloy fabricated by powder metallurgy route. *Lett. Mater.* **9**, 511–516 (2019). <https://doi.org/10.3390/met10121615>
 55. K. Ameyama, N. Horikawa, M. Kawabata, Unique mechanical properties of harmonic structure designed materials. *Tetsu-to-Hagane.* **105**, 124–126 (2019)
 56. H.R. Wenk, P. Van Houtte, Texture and anisotropy. *Rep. Prog. Phys.* **67**, s1367 (2004)
 57. J.W. Christian, *Proc. ICSSMA 2: 2nd Int. Conf. on Strength of Metals and Alloys Vol. 1*, ASM (1970) p. 29.
 58. M. Kawata. X-Ray analysis of residual stress and texture in ground carbon steels; Master theses; Toyohashi Univ. Tech., March 45–47, (1982).
 59. A. Biesiekierski, J. Wang, M. Abdel-Hady Gepreel, C. Wen, A new look at biomedical Ti-based shape memory alloys. *Acta Biomater.* **8**, 1661–1669 (2012). <https://doi.org/10.1016/j.actbio.2012.01.018>
 60. Y. Li, C. Yang, H. Zhao, S. Qu, X. Li, Y. Li, New developments of ti-based alloys for biomedical applications. *Materials.* **7**, 1709–1800 (2014). <https://doi.org/10.3390/ma7031709>
 61. M. Niinomi, Recent metallic materials for biomedical applications. *Metall. Mater. Trans. A.* **33**, 477–486 (2002). <https://doi.org/10.1007/s11661-002-0109-2>
 62. H.C. Hsu, S.C. Wu, Y.S. Hong, W.F. Ho, Mechanical properties and deformation behavior of as-cast Ti-Sn alloys. *J. Alloys Compd.* **479**, 390–394 (2009). <https://doi.org/10.1016/j.jallcom.2008.12.064>
 63. J.L. Murray. In :J. L.Murray (Ed.),*Alloy Phase Diagrams*, ASM International, Materials Park, Ohio, 1987, p. 294.
 64. W.D. Callister, *Materials Science and Engineering: An Introduction, Seventh ed* (Wiley, New York, 2007)
 65. T. Sato, S. Hukai, Y.C. Huang, The Ms points of binary titanium alloys. *J. Aust. Inst. Met.* **5**, 149–153 (1960)
 66. E. Gouvea, M. Lagos, A. Vicente, D. Lopez, I. Agote, J.A. Calero, V. Amigó, Ti-27Nb-8Mo Beta Alloy Developed by Electric Resistance Sintering. Euro PM 2019 – Spark Plasma Sintering.
 67. A. Amigó-Mata, E. Gouvea, M.A. Lagos, D. López, I. Jesús-Romero, I. Agote, A. Vicente-Escuder, J.A. Calero, Effect of ERS Process Parameters on the Microstructure and Mechanical Properties of Ti6Al4V, Euro PM2019 – Spark Plasma Sintering.
 68. E.P. Utomo, I. Kartika, A. Anawati, Effect of Sn on mechanical hardness of as-cast Ti-Nb-Sn alloys. (2018) <https://doi.org/10.1063/1.5038328>.
 69. S.S. Da Rocha, G.L. Adabo, G.E.P. Henriques, M.A. Nóbilo, Vickers hardness of cast commercially pure titanium and Ti-6Al-4V alloy submitted to heat treatments. *Braz. Dent. J.* **17**, 126–129 (2006). <https://doi.org/10.1590/s0103-64402006000200008>
 70. C.R.M. Afonso, K. Martinez-Orozco, V. Amigo, C.A.D. Rovere, J.E. Spinelli, C.S. Kiminami, Characterization, corrosion resistance and hardness of rapidly solidified Ni-Nb alloys. *J. Alloys Compd.* **829**, 154529 (2020). <https://doi.org/10.1016/j.jallcom.2020.154529>
 71. N. Mavros, T. Larimian, J. Esquivel, R.K. Gupta, R. Contieri, T. Borkar, Spark plasma sintering of low modulus titanium-niobium-tantalum-zirconium (TNTZ) alloy for biomedical applications. *Mater. Design.* **183**, 108163 (2019). <https://doi.org/10.1016/j.matdes.2019.108163>
 72. Q. Kong, X. Lai, X. An, W. Feng, C. Lu, J. Wu, C. Wu, L. Wu, Q. Wang, *Mater. Today Commun.* **23**, 101130 (2020). <https://doi.org/10.1016/j.mtcomm.2020.101130>
 73. F.E.T. Heakal, K.A. Awad, Electrochemical corrosion and passivation behavior of titanium and its Ti-6AL-4V alloy in low and highly concentrated HBr solutions. *Int. J. Electrochem. Sci.* **7**, 6539–6554 (2011)
 74. A.A. Ahmed, M. Mhaede, M. Wollmann, L. Wagner, Effect of micro shot peening on the mechanical properties and corrosion behavior of two microstructure Ti–6Al–4V alloy. *Appl. Surf. Sci.* **363**, 50–58 (2016). <https://doi.org/10.1016/j.apsusc.2015.12.019>

Publisher's Note Springer Nature remains neutral with regard to jurisdictional claims in published maps and institutional affiliations.